Feenstra, A., Rhede, D., Koch-Müller, M., Wiedenbeck, M., Heinrich, W. (2009): Hydrogen zoning in zinc-bearing staurolite from a high-P, low-T diasporite (Samos, Greece): A combined EMP-SIMS-FIB-FTIR study. - American Mineralogist, 94, 5-6, 737-745

DOI: 10.2138/am.2009.3107

Hydrogen zoning in zinc-bearing staurolite from a high-*P*, low-*T* diasporite (Samos, Greece): A combined EMP-SIMS-FIB-FTIR study

Anne Feenstra[1], Dieter Rhede, Monika Koch-Müller, Michael Wiedenbeck, and Wilhelm Heinrich*
GeoForschungsZentrum Potsdam, Department 3, Telegrafenberg, D-14473 Potsdam, Germany.
[1]Deceased on April 9, 2007.
*email: whsati@gfz-potsdam.de

ABSTRACT

Li-rich zincostaurolite occurs as millimeter-long crystals at the marble footwall of a meta-karstbauxite on eastern Samos. The Samos rocks have been metamorphosed during an early Alpine high-*P*, low-*T* metamorphism (M1) followed by a late Alpine greenschist-grade overprint (M2). Textures and mineral chemistry indicate that staurolite formed from gahnite, cookeite and pyrophyllite during the early M1 stage. Staurolite crystals show growth zoning with cores enriched in Zn. Concentrations of Fe, Mg, Co, and, to a minor extent, Li increase toward the rims.

Hydrogen concentrations were analyzed by SIMS. They are significantly higher in cores (up to 5.97 atoms H per 48 O) compared to rims (3.9 to 4.5 atoms H) and clearly negatively correlated with Al. Synchroton-light polarised FTIR spectra on oriented FIB-prepared foils show the same zonation effect, the absolute hydrogen concentrations being systematically lower by about 25%. The discrepancy is caused by sub-micrometer scale hydrogen loss at the crystal surface during FIB-thinning. This staurolite is unique as from the three available hydrogen sites the H3 site has the highest occupation ever observed, whereas the H2 site is not occupied. This is probably due to the high Li-content.

The zonation in hydrogen is interpreted as reflecting the two-stage growth. M1-staurolite that formed a low *T* of about 400-450 °C and high *P* of >1.5 GPa incorporated nearly the maximum amount of hydrogen allowed by the staurolite structure (6 H pfu) and was subsequently overgrown

and marginally replaced during the M2 stage by less hydrous, Fe-Co richer staurolite. Hydrogen zoning in staurolite is facilitated by the sensitivity of its structure to changing *P-T* conditions. Water in staurolite is maximized at high *P* and low *T*. Cores of staurolite from Samos represent the most hydrous staurolite compositions reported to date.

Keywords: Staurolite, hydrogen zoning, SIMS, FTIR, Metabauxite

INTRODUCTION

Staurolite is an important index mineral for determining the metamorphic grade of Al-rich rocks. It has a flexible structure and the crystal chemistry is complex (Holdaway et al. 1986a, 1986b, 1991, 1995; Dutrow et al. 1986; Dyar et al. 1991; Hawthorne et al. 1993a, 1993b, 1993c; Koch-Müller 1997; Koch-Müller et al. 1997, 1998; Chopin et al. 2003). This is due to variably occupied lattice sites resulting in various coupled vacancy-cation and other complex intracrystalline cation substitutions, which may induce local ordering. Further complexity arises from the fact that staurolite may incorporate highly variable amounts of hydrogen (e.g., Lonker 1983; Holdaway et al. 1986a). A special feature is that staurolite in zinci- and lithium-rich bulk compositions may accommodate large amounts of Zn and Li into the structure (e.g., Feenstra et al. 2003; Chopin et al. 2003, and references therein). Because both Zn and Li strongly partition into staurolite compared to other common Fe-Mg-Al silicates, this leads to considerable expansion of the staurolite stability field, both toward lower and higher metamorphic grades (e.g,. Feenstra et al. 2003).

The general formula of staurolite is $A_4B_4C_{16}D_4T_8O_{40}X_8$ (Hawthorne et al. 1993c). The structure can be considered as alternating oxide-hydroxide and kyanite-like layers. Three distinct octahedra (M) are present in each of these layers: M1A, M1B, and M2 in the kyanite layer, and M3A, M3B, and M4 in the oxide-hydroxide layer. The tetrahedral site of the kyanite layer is termed T1 and that of the oxide-hydroxide layer T2 (Hawthorne et al. 1993a). Preferential site occupations of the various cations and their relation to the general formula are given in Table 1 (Hawthorne et al.

1993c; see also Chopin et al. 2003). There is extensive work on the various coupled substitution mechanisms, both in natural and synthetic staurolites (cf. above). It has been shown, for example, that Zn-Fe substitution in staurolite is continuous (Griffen 1981) and that Li incorporation in T2 is restricted to a maximum of 1.5 apfu, calculated on the basis of 48 O (Dutrow 1991; Feenstra et al. 2003). However, correct formulation of the crystal chemistry and proper assignment of the cation sites are hampered by the fact that hydrogen concentrations are often not measured, and this is particularly true for natural staurolites that may exhibit chemical zoning. In absence of direct determinations, hydrogen concentrations are often estimated by considering the Si content and the <T1-O> distances measured by XRD (Hawthorne et al. 1993a) or by estimation from the CATSUM index (Hawthorne 1993c; see also Feenstra et al. 2003; Chopin et al. 2003). However, it would appear that complete analysis of all cations including hydrogen is the better choice, particularly if one takes into account that hydrogen contents are an important monitor of the pressure-temperature conditions of staurolite formation. For the FeAlSiOH system, Holdaway et al. (1995) have shown that hydrogen contents continuously increase with decreasing temperature and increasing pressure across the whole stability field of staurolite coexisting with aluminum silicate, and that its structure can accommodate a maximum amount of 6 H pfu. So far, no natural or experimental staurolite has been reported that actually approaches hydrogen contents that high, and measured or estimated values range from about 2 H pfu (e.g., Lonker 1983) to about 4.6 pfu (Holdaway et al. 1991).

Hydrogen in the staurolite structure is incorporated at three different sites: H1, H2 and H3 (Koch-Müller et al. 1995). The three possible sites are filled to variable extents. Detailed polarized infrared spectroscopy on Fe-rich staurolite from Pizzo Forno has shown that each of the three hydrogen types is bonded to the undersaturated O1 oxygen in the structure and that the corresponding OH dipoles are oriented along different directions. H1 occupation is associated with cation vacancies at M3, H2 with vacancies at T2, and H3, though of minor importance in Fe-rich staurolite, also with vacancies at T2 (Koch-Müller et al. 1995). It is, however, conceivable that significant Li-incorporation on T2 would affect amount and distribution of H atoms on H2 and H3,

respectively. There are various exchange vectors including charge-reducing substitutions that produce cation vacancies at M3 and T2 and concomitant H incorporation into H1 to H3 (e.g., Holdaway 1986b; Hawthorne et al. 1993c; Koch-Müller et al. 1995; Chopin et al. 2003). The important substitutions are:

(1) $^{[M3]}\square + 3\ H^{+} \Leftrightarrow {}^{[M3]}Al^{3+} + 3\ \square$ (hydrogens at H1)

(2) $^{[T2]}\square + 2\ H^{+} \Leftrightarrow {}^{[T2]}R^{2+} + 2\ \square$ (hydrogens at H2)

(3) $^{[T2]}Li^{+} + H^{+} \Leftrightarrow {}^{[T2]}R^{2+} + \square$

where Equation (3) applies to Li-rich staurolite. The site for the H atoms associated with Li incorporation is as yet unclear.

In this paper, we report the chemical composition of a natural metamorphic Li- and Zn-rich staurolite single crystal formed at low-temperature – high-pressure conditions. We present chemical zoning by detailed electron microprobe (EMP) work and secondary ion mass spectrometry (SIMS) by which lithium and hydrogen concentrations were quantified. Hydrogen contents, variable hydrogen distributions, and hydrogen substitution mechanisms are further investigated by synchroton-based Fourier transform infrared (FTIR) spectroscopy on oriented microfoils cut by focussed ion beam techniques, and results obtained from SIMS and FTIR methods are compared. We show that most of the H is incorporated as H1 along with vacancies at the M3 sites and that a remarkably high amount is present as H3, correlated with Li at T2. We highlight that extremely high H concentrations of up to 5.97 apfu and a very strong H zonation in the staurolite crystal are present, which is interpreted as reflecting changing *P*-*T* conditions during staurolite growth in low-temperature, high-pressure rocks.

STAUROLITE STUDIED

The investigated H-Li-rich zincostaurolite occurs at the marble footwall of a diaspore-bearing polymetamorphic meta-karstbauxite on the island of Samos, Greece. The petrogenesis of the staurolite-bearing rocks was reported in detail by Feenstra et al. (2003). In short, staurolite formed

from gahnite, cookeite, pyrophyllite, diaspore and minor Fe-oxide during early Alpine high-*P* metamorphism (M1-event) at peak conditions of about 450°C and >1.5 GPa. During late Alpine isothermal decompression staurolite partially equilibrated towards greenschist grade conditions (M2-event) and was partly replaced by gahnite, white Na-Ca-Li mica and minor amounts of Ni-chlorite, zincohögbomite, diaspore and Fe-Mn-(hydro)oxides. Here, we focus on the chemical zoning displayed by the staurolite crystals, aiming to link this zoning to the pressure-temperature evolution of the Samos rock. We selected rock sample Sa9a, which was previously described by Feenstra et al. (2003). Several staurolite grains were investigated. Here, we report on grain No. Sa9aE because it shows only minor indication of secondary replacement. Additional information is provided by grain No. Sa9aX from the same hand specimen, on which FTIR measurements have been performed.

ANALYTICAL METHODS

The separation procedure for staurolite from sample Sa9a was described elsewhere (Feenstra et al. 2003). For EMP and SIMS analysis, the grain was embedded in holes drilled into 1-inch diameter glass sample holders using the minimum possible amount of the epoxy resin.

EMP

The zoning in chemical composition of the staurolite crystal Sa9aE was determined by wavelength-dispersive analysis (WDS) techniques using a CAMECA SX100 instrument at GFZ Potsdam. Sixty-one spots were measured across the 261 μm wide profile V-W, and 36 spots across R-S (275 μm; Fig. 1). Solid inclusions were carefully avoided. Operating conditions were 15 kV accelerating potential, 10-20 nA beam current and a beam diameter of 1 to 2 μm. Typical peak counting times were 20-30 s for major and 20-60 s for minor elements; backgrounds were counted for 10-30 s. Standards included the following synthetic and natural minerals and metals: wollastonite (Si); rutile (Ti); corundum (Al); hematite (Fe); eskolaite (Cr); periclase (Mg); rhodonite (Mn); sphalerite (Zn);

NiO (Ni); metallic V and Co. The raw intensity data were corrected with the PAP program (Pouchou and Pichoir 1985). The quality and reproducibility of the analyses was continuously monitored by including well-characterized standards (staurolites, kyanite, feldspars) during the sessions. A selection of individual spot analyses is given in Table 2.

The staurolite grain Sa9aE was scanned by X-ray mapping using the same instrument. Element mapping was carried out in WDS mode moving the stage in steps of 1 µm using a beam current of 40 nA and counting times of 400 ms per step. Figure 1 shows variations in Zn, Fe, Ni and Co X-ray intensities across the entire grain.

SIMS

The Li and H concentrations were determined by secondary ion mass spectrometry (SIMS) with a CAMECA ims 6f instrument at GFZ Potsdam. A 3 nA mass-filtered primary $^{16}O^-$ beam was accelerated to 12.5 kV and focused to form a ~15 µm diameter beam at the sample surface. The secondary accelerating potential was 10 kV and the energy slit was set to a width corresponding to 50 V. The mass resolution (M/ΔM) was 2500. Energy filtering was applied to suppress molecular interferences (-75 V offset) and the measured $^1H^+$ and $^7Li^+$ intensities were normalized to $^{30}Si^+$. Counting times per cycle were 10 s for ^1H and 2 s for ^7Li and ^{30}Si. A 10-min pre-sputtering was applied to reduce surface contamination. Furthermore, improvements to the vacuum system and a sample holder that maintained the sample at liquid nitrogen temperatures were used. This suppresses any possible hydrogen vacuum contamination, which would adversely affect the detection limit for intra-crystalline H in specific, and which degrades overall data quality in general (Wiedenbeck et al. 2004).

For calibration, three natural standards were used, the H_2O and Li_2O contents of which are well known from independent analytical methods: staurolite sample 117189 containing 1.65 wt% H_2O and 0.05 wt% Li_2O (Holdaway et al. 1986a; Hawthorne et al. 1993a), staurolite sample St 77-55C containing 2.24 wt% H_2O and 0.56 wt% Li_2O (Dutrow et al. 1986; Holdaway et al. 1986a), and

cookeite (Vanoise; Vidal and Goffé 1991) containing 14 wt% H_2O and 2.45 wt% Li_2O (Vidal and Goffé 1991). A water-free kyanite from Naxos was additionally applied for the calibration curve of water. Plots of the $^{1}H^{+}/^{30}Si^{+}$ and $^{7}Li^{+}/^{30}Si^{+}$ ratios (with associated 1σ st.d. based on 15-16 spot analysis for each standard) vs. the independently determined H_2O and Li_2O concentrations result in linear relationships (Fig. 2). These were used to determine the H_2O and Li_2O concentrations of Sa9aE from Samos.

SIMS-profiles along V-W and R-S were measured at a distance of a few micometer parallel to the EMP profiles, using identical steps between the individual spots. Because SiO_2 concentrations in staurolite show almost no variations (Table 2; see also Holdaway et al. 1986) the count ratios of $^{1}H^{+}/\,^{30}Si^{+}$ and $^{7}Li^{+}/\,^{30}Si^{+}$ were used to determine the concentrations.

IR spectroscopy

The high absorption in the OH-stretching region requires very thin (< 10 μm) samples for IR measurements. Oriented staurolite foils were prepared in different ways. (1) 3 to 5 μm thick and 10 x 20 μm wide foils of Sa9aE were cut closely adjacent to the EMP and SIMS traverses using FIB techniques (Wirth 2004), by applying a Ga-ion beam at 30 kV and 2.7 nA. The beam current of 2.7 nA was about four times higher than that used for routinely prepared thin foils of 120 nm thickness. Foils of Sa9aE were taken close to core and rim (a and b in Fig. 1) and included foils of different orientations, namely films containing the crystallographic *a* and *c* axes, i.e., (010) films, and one film that contained the *b* and *c* axes, i.e., a (100) film. The exact orientation of the films was determined by TEM on additional foils that had a thickness of 120 nm and were 10 x 20 μm wide. (2) Staurolite grain number Sa9aX from the same hand specimen and having similar dimensions was optically oriented to the same directions as above, embedded in special IR transparent wax (Apiezon), and thinned by conventional polishing down to about 10 μm. We were not able to prepare intact whole grain slices with such method, but obtained several small oriented fragments of core and rim that were accessible for IR measurements. And (3), foils of staurolite from Pizzo Forno

were cut to the same orientations using identical FIB conditions as for Sa9aE. The thicknesses of these foils were 3.2 μm, 6.1 μm, and 7.4 μm, respectively. Pizzo Forno staurolite is extensively used as standard, is homogeneous with respect to water concentrations, and has a well-known absolute content of 2.05 wt% H_2O (e.g., Koch-Müller and Langer 1998).

Polarized FTIR spectra of thin films and polished samples were obtained at the synchroton IR-beamline at BESSY II (Berlin, Germany) using a Nicolet 870 FTIR spectrometer with KBr beamsplitter equipped with a Continuum microscope and MCT detector. Spectra were always collected from inclusion-free regions. Apertures ranged from 8 x 5 μm to about 10 x 15 μm for the foils, and 14 x 14 μm for the polished sample fragments. Spectra were averaged over 256 scans with a resolution of 4 cm^{-1}. For quantification of hydrogen we applied the IR calibration for water in Fe-rich staurolite ($e_{i,tot}$ = 83 000 $L/mol_{H2O}/cm^2$; Koch-Müller and Langer 1998). Because absorption coefficients are strongly dependent on the wavenumber of the corresponding OH bands and as OH band positions in Zn-staurolite are different to those in Fe-rich staurolites we also calculated specific absorption coefficients for our Zn- and Li-rich staurolite applying the general calibration formula of Libowitzky and Rossman (1997). For the band at 3542 cm^{-1} we get a value of 52 000 $L/mol_{H2O}/cm^2$ and for that at 3456 cm^{-1} (plus the shoulder at the low energy side of this band) a value of 80 000 $L/mol_{H2O}/cm^2$. These specific coefficients were used for hydrogen quantification at the different sites.

RESULTS

Staurolite chemistry

Representative analyses along profiles V-W and S-R are given in Table 2. Staurolite formulae were calculated on the basis of 48 O atoms and concentrations of all elements in terms of atoms per formula unit (apfu) vs. distance are shown in Figure 3. Dyar et al. (1991) showed by Mössbauer spectroscopy that in oxidized rocks about 7% of the total iron in staurolite is ferric. Staurolite Sa9aE

is poor in total iron and accounting for ferric iron would have only a minor effect on the calculated structural formulae. Thus, all of the iron is calculated as Fe^{2+}. In Table 2, the mole fraction of the i^{th} element (i = Fe^{2+}, Mg, Mn^{2+}, Zn, Ni, Co, Li) is calculated as $X_i = \sum R^{2+} + Li$.

Sa9aE is a Li-rich zincostaurolite and compositionally zoned (Fig. 3). Zinc is the dominant divalent cation. ZnO concentrations amount to 12.54 wt% in the core and 9.60 wt% in the rim, corresponding to X_{Zn} of 0.65 and 0.49, respectively. FeO concentrations range from 0.77 wt% (core) to 2.33 wt% (rim), corresponding to X_{Fe} of 0.05 and 0.14. FeO contents are clearly negatively correlated with ZnO contents. With regard to Zn and Fe, cores show a large flat plateau, which is symmetrical across S-R, slightly asymmetrical across V-W, and a ~ 50 μm wide rim on either side. Li concentrations are high, but the zoning is much less pronounced in that concentrations in the core are somewhat lower (S-R: Li_2O = 0.89 wt%, X_{Li} = 0.25; V-W: Li_2O = 0.98 wt%, X_{Li} = 0.28) than in the rims (S-R: Li_2O = 1.01 wt%, X_{Li} = 0.28; V-W: Li_2O = 1.23 wt%, X_{Li} = 0.33). The staurolite is very poor in Mg (0.12 to 0.31 wt% MgO; X_{Mg} = 0.01 to 0.03) and Mn (0.06 to 0.27 wt% MnO; X_{Mn} = 0.01 to 0.02), and there is no detectable zoning with respect to Mg and Mn. Nickel, Co, Cr, and Ti display maximum values at the inner side of the rim and decrease toward the outer part of the rim (Figs. 1 and 3). Maximum concentrations amount to 0.45 wt% of NiO, 0.44 wt% of CoO, 0.27 wt% of Cr_2O_3, and 0.04 wt% of TiO_2. Concentrations of V and F are below the EMP detection limit.

Staurolite Sa9aE is rich in Si (7.86 to 8.06 apfu; average 7.96 apfu, n = 99 spots) despite the fact that it occurs in a Si-undersatured, Al-saturated diaspore-bearing rock. There is virtually no Si-zoning. Incorporation of Al on the T1 site is therefore very low, with 0.04 apfu on average. The most striking feature is the very high hydrogen concentration, the pronounced H zonation, and the inverse coupling of H and Al contents (Fig. 3). Profile V-W shows a maximum H concentrations of 5.97 apfu in the core that continuously decrease to 4.4 apfu at a distance of about 80 μm on either side of the maximum. Toward the rims, H concentration slightly increases again to about 4.6 apfu, finally dropping to 3.8 apfu at the right-hand side of the profile. Profile S-R displays a broad plateau

in the core with hydrogen concentrations of about 5.2 ± 0.2 apfu, and decreasing contents to the rims (4.6 apfu, left-hand side; 4.8 apfu, right-hand side). Values of 5.97 and 5.2 apfu correspond to concentrations of 3.25 and 2.86 wt% H_2O, respectively, and these are by far the highest hydrogen contents in staurolite reported as yet. Hydrogen concentrations and zoning are negatively correlated with Al contents, as is clearly displayed in both profiles. Minimum concentrations of Al attain 17.13 apfu in the core and maximum concentrations reach 17.65 apfu in the rim. Figure 4 shows H vs. Al concentrations of all 99 analyses spots. The slope of the regression curve is -3.51 ($r^2 = 0.74$), suggesting that $3H^+ + {}^{[M3]}\square \Leftrightarrow 3\square + {}^{[M3]}Al^{3+}$ is the main, though not the only coupled exchange mechanism for H incorporation. Hydrogen incorporation only at the H1 site is coupled with vacancies at M3. Another substitution mechanism would require occupation of the H2 and/or H3 sites, which can be assessed by IR-spectroscopy.

Hydrogen concentrations measured by FTIR

Polarized IR spectra of the FIB-prepared foils from Sa9aE were measured with E//*a* and E//*c* and are presented in Figures 5a (core) and 5b (rim). Similarly, Figure 5c shows polarized spectra of polished fragments of core and rim from Sa9aX. All films show identical IR patterns. Each spectrum consists of two OH vibration bands: one with the main absorption with E//*a* at 3456 cm^{-1} plus a shoulder at the low energy side and one at 3542 cm^{-1} with an isotropic absorption behavior. One spectrum was measured with E//*b* (not shown in Fig. 5); here all bands have zero intensity. The observed bands are assigned using the classification of Koch-Müller et al. (1995, 1997): the band at 3456 cm^{-1} is assigned to the vibration of the O1-H1 dipole, the one at 3543 cm^{-1} to the O1-H3 dipole; there are no bands in the region at 3677 cm^{-1}, indicating that in our Li-Zn-rich staurolite vibrations of the O1-H2 dipole are absent (Koch-Müller et al. 1995, 1997). This is in line with spectra of synthetic zincostaurolite where configurations involving H2 vibrations are also missing (Koch-Müller et al. 1997).

Figures 5a-5c clearly show that for both grains the band intensities are higher in the cores than

in the rims, thus reflecting their higher H concentrations. Using the absorption coefficient of Koch-Müller and Langer (1998) for Fe-staurolite, the fragments of grain Sa9aX yield 2.3 wt% H_2O for the rim, and 2.8 wt % H_2O for the core. If the specific absorption coeffcients calculated by the Libowitzky and Rossman (1997) method are used, somewhat higher concentrations result, namely 2.6 wt% H_2O for the rim, and 3.2 wt% H_2O for the core. Specific absorption coefficients of Libowitzky and Rossman (1997) allow for quantification of the H concentrations in H1 and H3 separately. Using these, 76% of the H sits at H1, and 24% at H3, in the core as well as in the rim.

When we apply the absorption coefficients as above to the spectra from the foils of grain Sa9aE prepared by FIB techniques (Fig 5a and b), similar H gradients result, but absolute values are lower by about 25% relative compared to those obtained by SIMS on the same sample. This discrepancy was resolved by analyzing spectra of FIB-prepared foils from Pizzo Forno Fe-staurolite standard. Applying the calibration of Koch-Müller and Langer (1998) for Fe-staurolite, spectra taken both at E//a and E//c also yield considerably less H_2O than the true value. Figure 5d shows the absorbance values of the Pizzo Forno staurolite standard vs. thickness, (1) of the conventionally polished samples (closed symbols), and (2) of the FIB-prepared foils (open symbols). The thickness of the latter was measured using the FIB-integrated FEI software. The straight lines indicate the linear relationship between the absorbance values of the standard and the thickness, and thus represent the true absorbance values for <11 μm thick samples (for details see Koch-Müller et al. 1998). The FIB-prepared foils do not plot onto this line. This is interpreted as resulting from hydrogen loss during FIB-thinning. Irrespective of the actual thickness, subtraction of about 2 μm (1 μm on each side) is required to obtain the effective thickness of the foil, i.e., the correct absorbance (arrows in Fig. 5d). This correction is applied to our spectra from Sa9aE. Using the absorption coefficent of Koch-Müller et al. (1997), we obtain 2.73 wt% H_2O for the core, and 1.96 wt% H_2O for the rim. Using the specific absorption coefficients of water (see above) again yields somewhat higher concentrations of 3.14 wt H_2O for the core and 2.28 wt H_2O for the rim. Again, 70

to 75% of the H are incorporated as H1, the remaining as H3.

Hydrogen concentrations obtained by SIMS were 3.25 wt% H_2O for the core and 2.07 to 2.49 wt% H_2O for the rim. Thus, H concentrations obtained by both methods agree fairly well, particularly with respect to the H concentration gradient. It would also appear that the specific absorption coefficients for Li-Zn-rich staurolite calculated after Libowitzky and Rossman (1997) provided the more accurate values for H concentrations. This holds also for concentrations of grain Sa9aX, for which no SIMS data are available.

DISCUSSION

Hydrogen incorporation mechanisms

The infrared spectra (Fig. 5a and b) and the slope of the inverse correlation of aluminum vs. hydrogen of -3.51 (Fig. 4) imply that hydrogen is not incorporated only via the exchange vector shown in Equation 1:

$$^{[M3]}\square + 3\,H^{+} \Leftrightarrow {}^{[M3]}Al^{3+} + 3\,\square$$

that puts H at the H1 site. An additional mechanism must exist. The IR spectra clearly revealed that the H2 site is unoccupied; instead significant amounts of H are located on H3. The intensity of the corresponding OH band is the highest observed ever in staurolite so far. Koch-Müller et al. (1995) concluded that in Fe-rich staurolite from Pizzo Forno H at H3 is bonded to O1 and forms a bifurcated hydrogen bridge to two adjacent O5 in a vacant T2 site. Staurolite Sa9aE, however, is characterized by a very small amount of vacancies and a very high amount of Li^{+} at T2 (Tables 1 and 2). Therefore, it is reasonable to assign the H3 band in our Li-rich staurolite in the same way, i.e., H is bonded to O1 and forms a bifurcated hydrogen bridge to two O5 in a T2 tetrahedron, which is not vacant but occupied by Li^{+}. Based on the crystal structure data for staurolite of Comodi et al. (2002), the estimated atomic coordinates for hydrogen at H3 are 0.35 (x) 0.00 (y) 0.59 (z). With this assignment the hydrogen incorporation at H3 is coupled with Li^{+} according to the

exchange vector gven in Equation 3 previously

$$^{[T2]}Li^{+} + H^{+} \Leftrightarrow {}^{[T2]}R^{2+} + \square$$

The simultaneous occupation of T2 by Li^{+} and H is possible because the distance between H and Li is large enough (1.96 Å).

That the substitution mechanism (3) is effective for H incorporation at H3 gains further plausibility when IR and SIMS results are compared. About 25% of the total H is located at H3. Recalculating the H contents from 94 analysis spots to 25% of their absolute values (excluding the three spots with the highest H contents), concentrations between 0.93 to 1.30 H pfu result. The corresponding Li concentrations are between 0.98 and 1.31 (see also Table 2), in a very similar range. On average, total Li concentrations appear to be slightly higher than that calculated for H at H3. This possibly implies an additional coupled substitution for Li incorporation of the type

$$(4) \quad ^{[T2]}Li^{+} + 0.33\ ^{[M3]}Al^{3+} \Leftrightarrow {}^{[T2]}Fe^{2+} + 0.33\ ^{[M3]}\square.$$

Dutrow (1991) has experimentally shown that this mechanism may occur to a relatively large extent. However, because IR spectra only allow for a rough estimation of the H distribution between the H1 and H3 sites, it is not clear wether the latter coupled substitution in our Li-Zn-rich staurolite is effective.

Hydrogen concentrations as a petrogenetic indicator

The shape of the H zonation profiles (Fig. 3) and the fact that H incorporation on H1 is inversely coupled with Al concentrations rules out diffusive H loss as possible mechanism for lower H concentrations inthe staurolite rims. We therefore consider the observed profiles as resulting from growth zonation.

The petrogenetic study of Feenstra et al. (2003) has shown that the staurolite-bearing metabauxite from Samos is a high-pressure, low-temperature rock. It was equilibrated during Early Tertiary peak metamorphism at 400 to 450°C, P > 1.5 GPa and subsequently overprinted during Tertiary decompression at greenschist facies conditions at 0.2 to 0.4 GPa at similar temperatures. In

a very detailed analysis of the thermodynamic properties of stoichiometric staurolite in the Fe-Al-Si-O-H system, Holdaway et al. (1995) demonstrated that the composition of staurolite coexisting with aluminum silicate in the *P-T* space can be contoured for H content. Hydrogen concentrations increase with pressure and decrease with temperature. The contours of the H isopleths calculated for staurolite solid solutions along the $H_2Fe_4Al_{18}Si_8O_{48}$ – $H_6Fe_2Al_{18}Si_8O_{48}$ join coexisting with Al_2SiO_5 + quartz + water are shown in Figure 6. Extrapolating the hydrogen isopleths calculated for the FASH system to conditions of the Samos rock, i.e., to 400 to 450°C, 1.5 GPa, and 0.2 to 0.4 GPa at the same temperature range, respectively, perfectly matches with the hydrogen concentrations of core (5.5 to 5.9 pfu) and rim (3.9 to 4.5 pfu) of our Samos staurolite (Fig. 6). One may argue that this is fortuitous because Sa9aE is an Fe-poor, Li-rich zincostaurolite where different H incorporation mechanisms are effective, and because the Samos assemblage is a diaspore-bearing, quartz-undersaturated rock while the calculations of Holdaway et al. (1995) hold for quartz + Al_2SiO_5-bearing assemblages. The true reason for this coincidence remains unclear as long as no thermodynamic data for Li and Zn-bearing phases are available. Nevertheless, from the close similarities of the two systems it is reasonable to assume that the extremely high H contents of the cores reflect early growth of staurolite during high-*P* – low-*T* conditions. Accordingly, and because diffusive H loss is excluded, the lower H content of the rims is interpreted as subsequent growth during later decompression. If one follows this interpretation, Sa9aE highlights the large effect that changing *P-T* conditions may exert on H incorporation into staurolite, and that very high H contents in staurolite cores may be preserved during the rock uplift history, at least as long as lower greenschist facies conditions are not exceeded.

ACKNOWLEDGMENTS

We thank G. Berger for sample polishing, O. Appelt for microprobe assistance, R. Wirth for cutting FIB foils, and M. Holdaway for providing staurolite standards. U. Schade is thanked for the help with the synchrotron IR measurements at BESSY II, Berlin. We acknowledge insightful reviews by C. Chopin and G. Della Ventura, as well as efficient editorial handling by G.D. Gatta.

REFERENCES CITED

Chopin, C., Goffé B., Ungaretti, L., and Oberti, R. (2003) Magnesiostaurolite and zincostaurolite: Mineral description with a petrogenetic and crystal-chemical update. European Journal of Mineralogy, 15, 167-176.

Comodi, P., Montagnoli, M., Zanazzi, P.F., and Boffa Ballaran, T. (2002) Isothermal compression of staurolite: A single-crystal study. American Mineralogist, 87, 1164-1171.

Dutrow, B.L. (1991) The effects of Al and vacancies on Li substitution in iron staurolite: A synthesis approach. American Mineralogist, 76, 42-48.

Dutrow, B.L., Holdaway, M.J., and Hinton, R.W. (1986) Lithium in staurolite and its petrologic significance. Contributions to Mineralogy and Petrology, 94, 496-506.

Dyar, M.D., Perry, C.L. Rebbert, C.R., Dutrow, B.L., Holdaway, M.J., and Lang, H.M. (1991) Mössbauer spectroscopy of synthetic and naturally occurring staurolite. American Mineralogist, 76, 27-41.

Feenstra, A., Ockenga, E., Rhede, D., and Wiedenbeck, M. (2003) Li-rich zincostaurolite and its decompression-related breakdown products in a diaspore-bearing metabauxite from East Samos (Greece): An EMP and SIMS study. American Mineralogist, 88, 789-805.

Griffen, D.T. (1981) Synthetic Fe/Zn staurolites and the ionic radius of $^{IV}Zn^{2+}$. American Mineralogist, 66, 932-937.

Hawthorne, F.C., Ungaretti, L., Oberti, R., Caucia F., and Callegari, A. (1993a) The crystal chemistry of staurolite: I. Crystal structure and site populations. Canadian Mineralogist, 31, 551-582.

———— (1993b) The crystal chemistry of staurolite: II. Order-disorder and the monoclinic orthorhombic phase transition. Canadian Mineralogist, 31, 583-595.

———— (1993c) The crystal chemistry of staurolite: III. Local order and chemical composition. Canadian Mineralogist, 31, 597-616.

Holdaway, M.J., Dutrow, B.L., and Shore, P. (1986a) A model for the crystal chemistry of

staurolite. American Mineralogist, 71, 1142-1159.

Holdaway, M.J., Dutrow, B.L., Borthwick, J., Shore, P., and Harmon, R.S. (1986b) H content of staurolite as determined by H extraction line and ion microprobe. American Mineralogist, 71, 1135-1141.

Holdaway, M.J., Mukhopadhyay, B., Dyar, M.D., Dutrow, B.L., Rumble III, D., and Grambling, J.A. (1991) A new perspective on staurolite crystal chemistry: Use of stoichiometric and chemical end-members for a mole fraction model. American Mineralogist, 76, 1910-1919.

Holdaway, M.J., Mukhopadhyay, B. ,and Dutrow, B.L. (1995) Thermodynamic properties of stoichiometric staurolite $H_2Fe_4Al_{18}Si_8O_{48}$ and $H_6Fe_4Al_{18}Si_8O_{48}$. American Mineralogist, 80, 520-533.

Koch-Müller, M. (1997) Experimentally determined Fe-Mg exchange between synthetic staurolite and garnet in the system MgO-FeO-Al_2O_3-SiO_2-H_2O. Lithos, 41, 185-212.

Koch-Müller, M. and Langer, K. (1998): Quantitative IR-spectroscopic determination of the component H_2O in staurolite. European Journal of Mineralogy, 10, 1267-1273.

Koch-Müller, M., Langer, K., and Beran, A. (1995) Polarized singel-crystal FTIR-spectra of natural staurolite. Physics and Chemistry of Minerals, 22, 108-114.

Koch-Müller M., Langer, K., Behrens, H., and Schuck, G. (1997) Crystal chemistry and infrared spectroscopy in the OH-stretching region of synthetic staurolites. European Journal of Mineralogy, 9, 67-82.

Koch-Müller, M., Kahlenberg, V., Bubenick, W., and Gottschalk, M. (1998) Crystal-structure refinement of synthetic Fe- and Mg-staurolite by Rietveld analysis of X-ray powder-diffraction data. European Journal of Mineralogy, 10, 453-460.

Libowitzky, E. and Rossman, G.R. (1997) An IR absorption calibration for water in minerals. American Mineralogist, 82, 1111-1115.

Lonker, S.W. (1983) The hydroxyl content of staurolite. Contributions to Mineralogy and Petrology, 84, 36-42.

Pouchou, J.L, and Pichoir (1985) PAP procedure for improved quantitative analysis. Microbeam Analysis, 20, 104-106.

Vidal, O. and Goffé, B. (1991) Cookeite $LiAl_4(Si_3Al)O_{10}(OH)_8$: Experimental study and thermodynamic analysis of its compatibility relations in the Li_2O-Al_2O_3-SiO_2-H_2O system. Contributions to Mineralogy and Petrology, 108, 72-81.

Wiedenbeck, M., Rhede, D., Lieckefett, R., and Witzki, H. (2004) Cryogenic SIMS and its applications in the Earth sciences. Applied Surface Science, 231-232, 888-892.

Wirth, R. (2004) A novel technology for advanced application of micro- and nanoanalysis in geosciences and applied mineralogy, European Journal of Mineralogy, 16, 863-876.

FIGURE CAPTIONS

Figure 1. Back-scattered electron micrograph and X-ray element maps for Zn, Fe, Ni, and Co of staurolite crystal Sa9aE, embedded in epoxy. The central part of the crystal contains numerous inclusions of Ca- (Fe, Mn, Mg) carbonate and a few paragonite (pg) solid inclusions. V-W and R-S indicate profiles along which EMP and SIMS analyses have been performed. Boxes labeled a and b denote locations where FIB-foils have been cut (see IR-spectra Figs. a and b).

Figure 2. (**a**) $^{1}H^{+}/^{30}Si^{+}$ ratios vs. H_2O concentrations, (**b**) $^{7}Li^{+}/^{30}Si^{+}$ ratios vs. Li_2O concentrations of reference samples staurolite 117189, staurolite 77-55C, and cookeite. Isotopic ratios measured by SIMS, H_2O and Li_2O by independent methods. Resulting regression lines were used to calculate the H_2O and Li_2O concentrations along profiles V-W and R-S of Sa9aE. Water-free kyanite was additionally used for determination of the $^{1}H^{+}/^{30}Si^{+}$ calibration curve. Error bars are 1σ; n ≥ 15 spots for each sample.

Figure 3. Variations in major and trace elements of staurolite Sa9aE along profiles V-W (**a**) and S-R (**b**) (cf. Fig. 1). Atoms calculated on the basis of 48 O atoms. H and Li measured by SIMS, all other elements by EMP.

Figure 4. Hydrogen vs. Al concentrations of all 99 spots along profiles V-W and S-R, calculated on 48 O atoms. Hydrogen incorporation is inversely coupled to Al. The slope of the regression curve is -3.51, suggesting that $3H^{+} + {}^{[M3]}❑ \Leftrightarrow 3❑ + {}^{[M3]}Al^{3+}$ is the main, though not the only coupled exchange mechanism for H incorporation.

Figure 5. (**a-c**) Polarized IR-spectra of staurolite Sa9aE, measured with E//*a* and E//c, respectively. (**a**) FIB-prepared sample from core (normalized to an effective thickness of 10 μm). (**b**) FIB-prepared sample from rim (normalized to an effective thickness of 10 μm). (**c**) Conventionally polished samples (10 μm thickness) from core (2.8 wt% H_2O) and rim (2.3 wt% H_2O). **a**,**b,** and **c**

measured by synchroton IR at Bessy II. (**d)** Closed symbols show the integral absorbance of OH modes vs. thickness of the Pizzo Forno staurolite standard (2.05 wt% H_2O), with E//a (circles) and E//c (squares). Data are from Koch-Müller and Langer (1998). Straight lines indicate the linear relationship between absorbance and thickness of the standard (Koch-Müller and Langer 1998). Open symboles (circles for E//a, squares for E//c) denote FIB-prepared foils. For correct H concentrations, a thickness correction of about 2 μm would be required due to H loss during FIB thinning.

Figure 6. *P-T* plot indicating M1 and M2 stage metamorphic conditions of the Samos rocks, along with H contents (pfu) of core and rim from staurolite Sa9aE. Also given are isopleths of H contents of Fe-staurolite coexisting with kyanite or sillimanite and water (data from Holdaway et al. 1995).

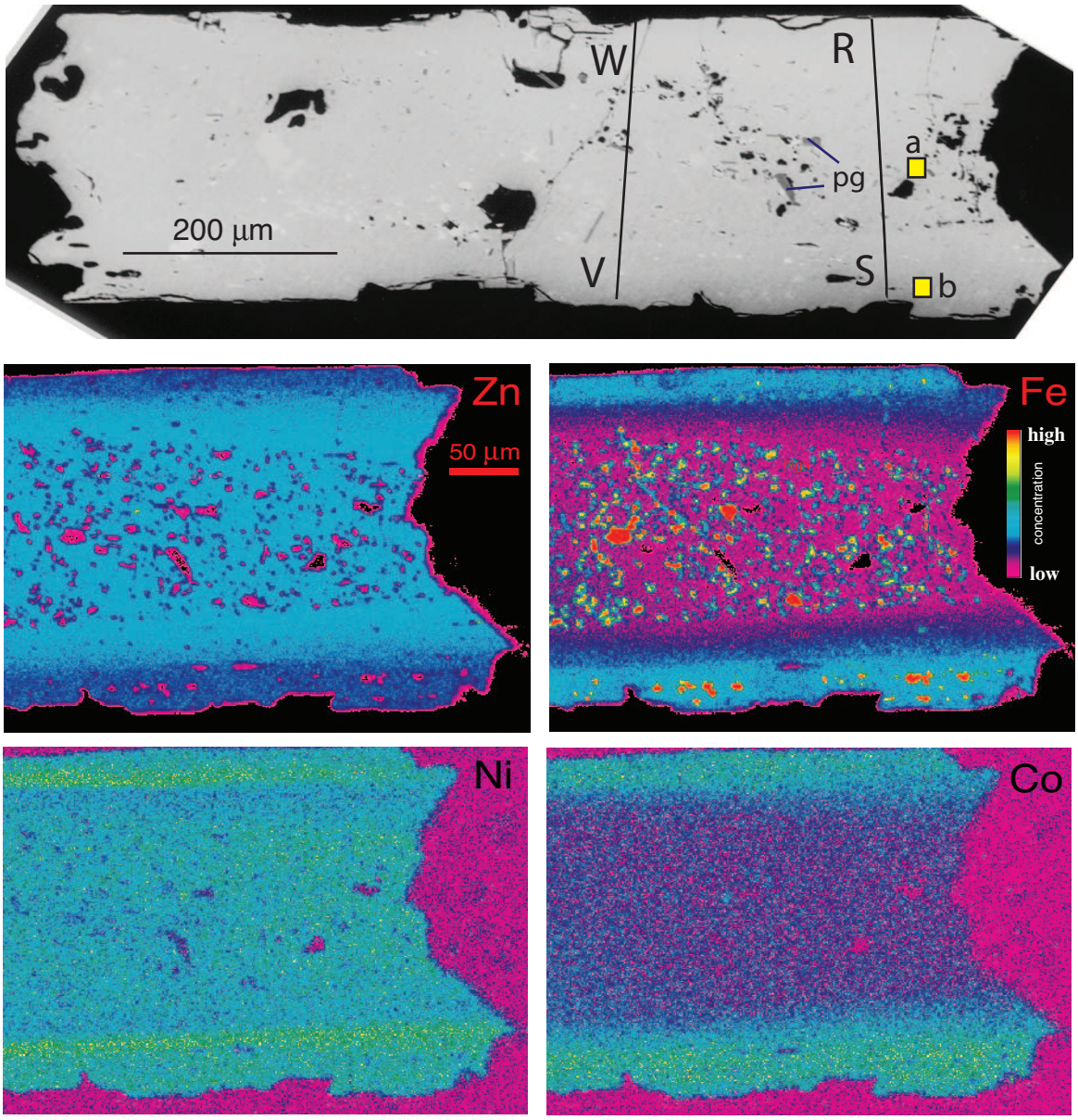

Figure 1. Back-scattered electron micrograph and X-ray element maps for Zn, Fe, Ni, and Co of staurolite crystal Sa9aE, embedded in epoxy. The central part of the crystal contains numerous inclusions of Ca- (Fe, Mn, Mg) carbonate and a few paragonite (pg) solid inclusions. V-W and R-S indicate profiles along which EMP and SIMS analyses have been performed. Boxes labeled a and b denote locations where FIB-foils have been cut (see IR-spectra Figs. a and b).

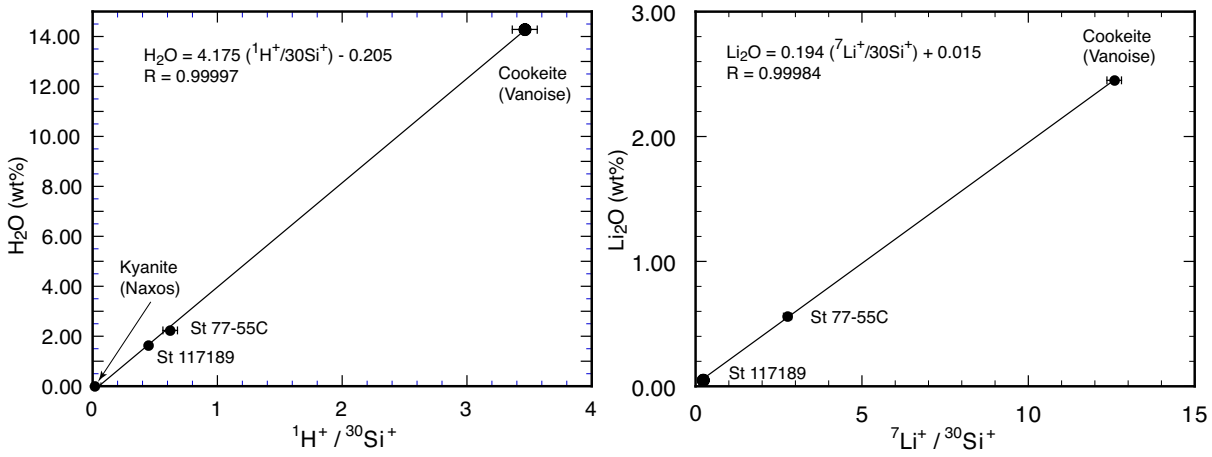

Figure 2. (**a**) $^{1}H^{+}/^{30}Si^{+}$ ratios vs. H_2O concentrations, (**b**) $^{7}Li^{+}/^{30}Si^{+}$ ratios vs. Li_2O concentrations of reference samples staurolite 117189, staurolite 77-55C, and cookeite. Isotopic ratios measured by SIMS, H_2O and Li_2O by independent methods. Resulting regression lines were used to calculate the H_2O and Li_2O concentrations along profiles V-W and R-S of Sa9aE. Water-free kyanite was additionally used for determination of the $^{1}H^{+}/^{30}Si^{+}$ calibration curve. Error bars are 1σ; n ≥ 15 spots for each sample.

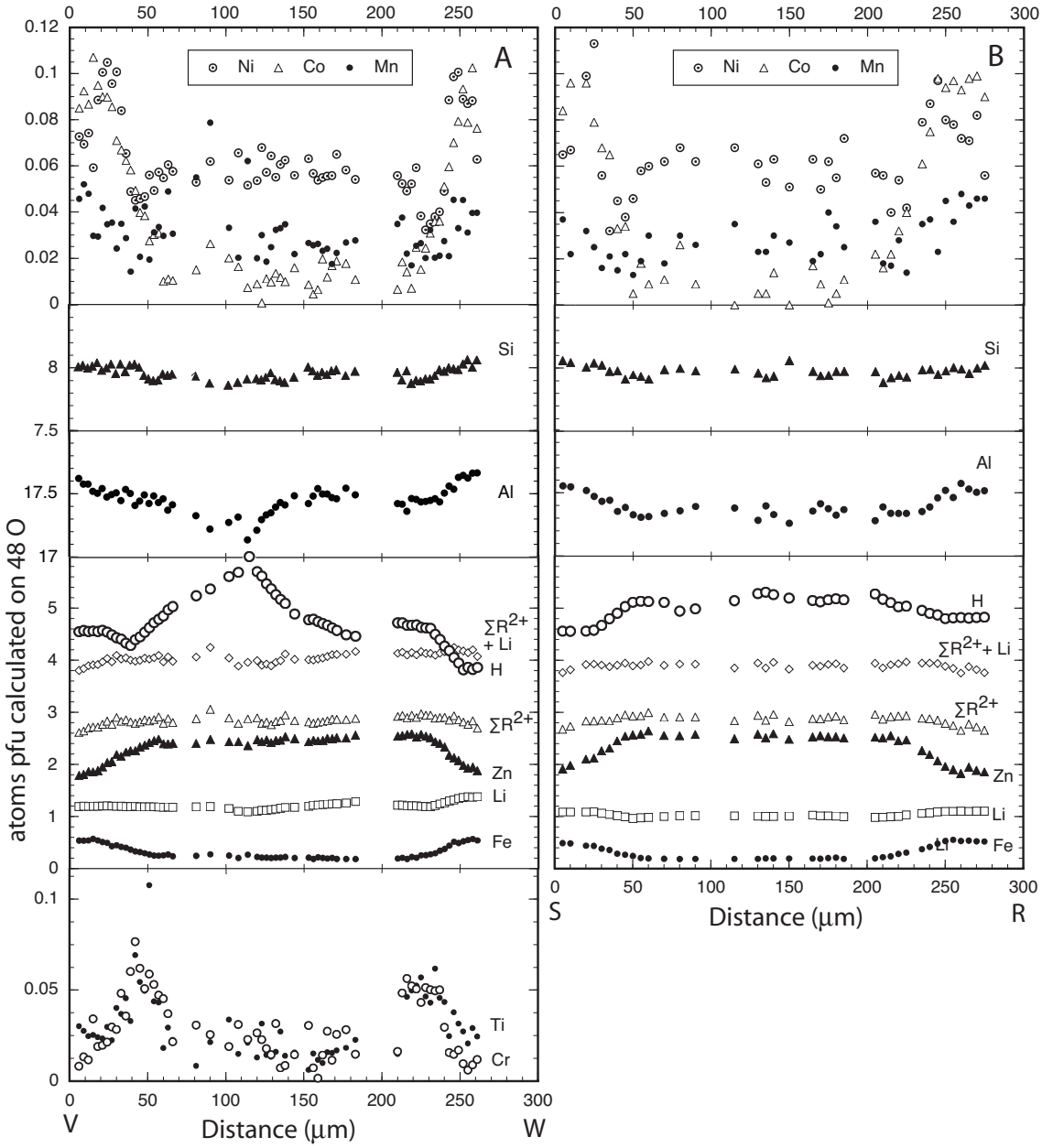

Figure 3. Variations in major and trace elements of staurolite Sa9aE along profiles V-W (**a**) and S-R (**b**) (cf. Fig. 1). Atoms calculated on the basis of 48 O atoms. H and Li measured by SIMS, all other elements by EMP.

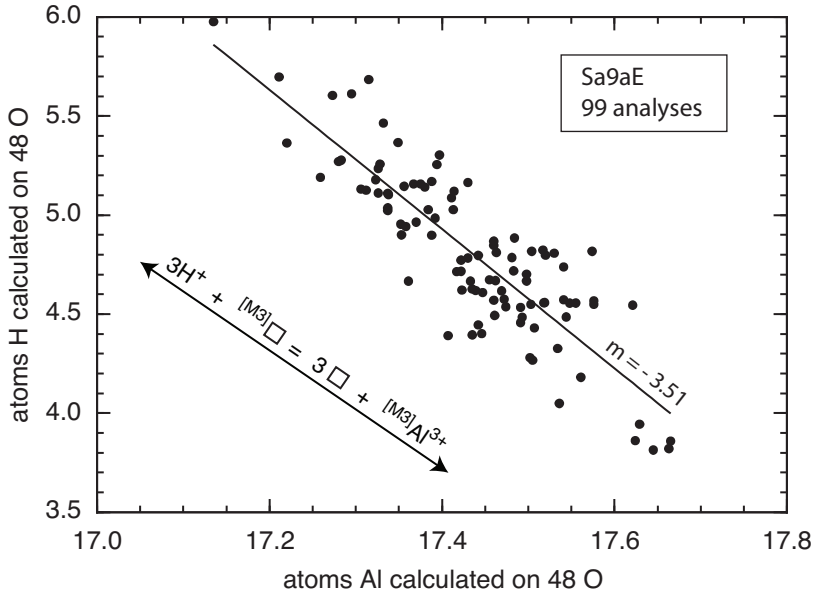

Figure 4. Hydrogen vs. Al concentrations of all 99 spots along profiles V-W and S-R, calculated on 48 O atoms. Hydrogen incorporation is inversely coupled to Al. The slope of the regression curve is -3.51, suggesting that $3H^{+} + {}^{[M3]}\square \Leftrightarrow 3\square + {}^{[M3]}Al^{3+}$ is the main, though not the only coupled exchange mechanism for H incorporation.

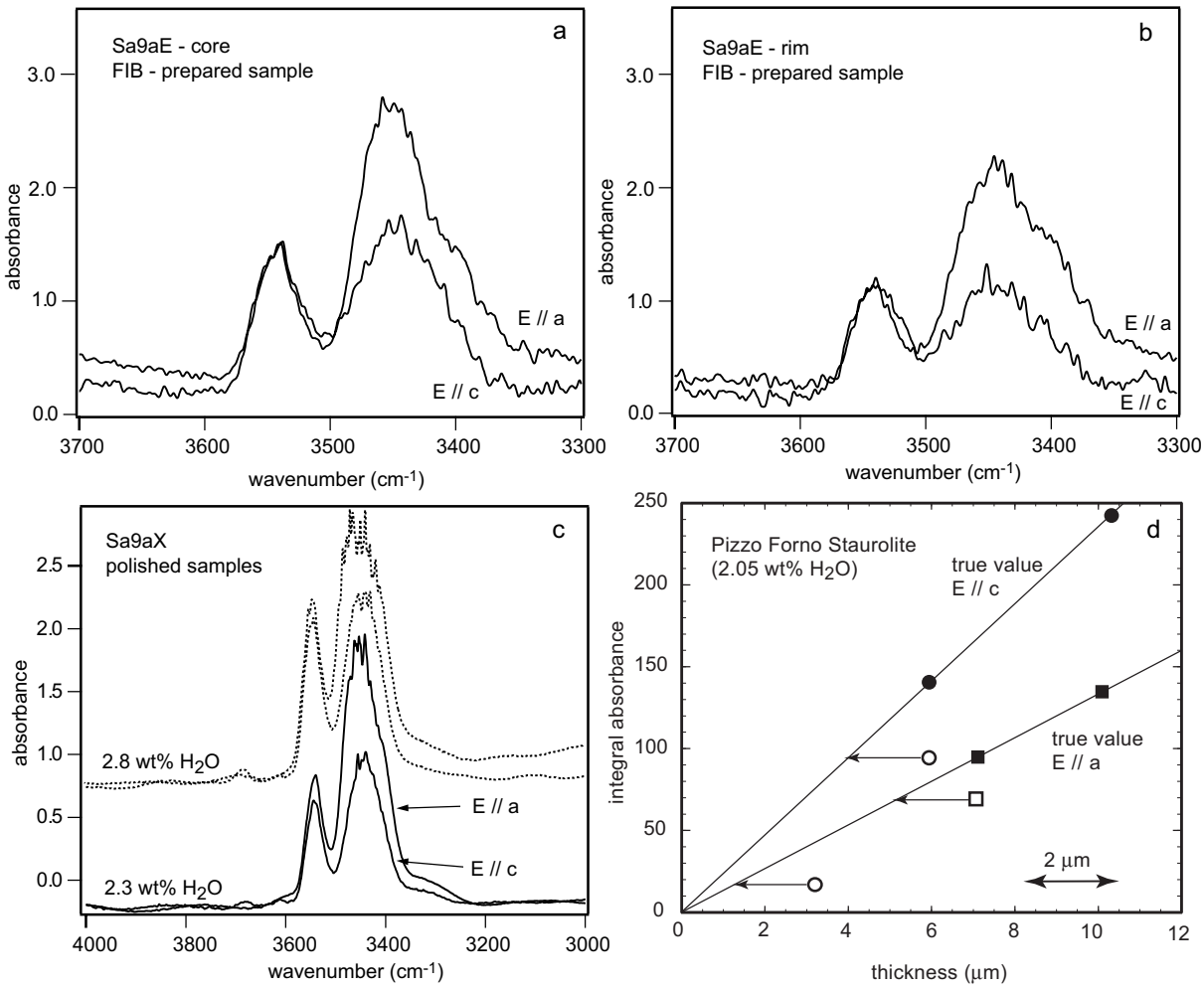

Figure 5. (**a-c**) Polarized IR-spectra of staurolite Sa9aE, measured with E//*a* and E//c, respectively. (**a**) FIB-prepared sample from core (normalized to an effective thickness of 10 µm). (**b**) FIB-prepared sample from rim (normalized to an effective thickness of 10 µm). (**c**) Conventionally polished samples (10 µm thickness) from core (2.8 wt% H_2O) and rim (2.3 wt% H_2O). **a**,**b,** and **c** measured by synchroton IR at Bessy II. (**d)** Closed symbols show the integral absorbance of OH modes vs. thickness of the Pizzo Forno staurolite standard (2.05 wt% H_2O), with E//a (circles) and E//c (squares). Data are from Koch-Müller and Langer (1998). Straight lines indicate the linear relationship between absorbance and thickness of the standard (Koch-Müller and Langer 1998). Open symboles (circles for E//a, squares for E//c) denote FIB-prepared foils. For correct H concentrations, a thickness correction of about 2 µm would be required due to H loss during FIB thinning.

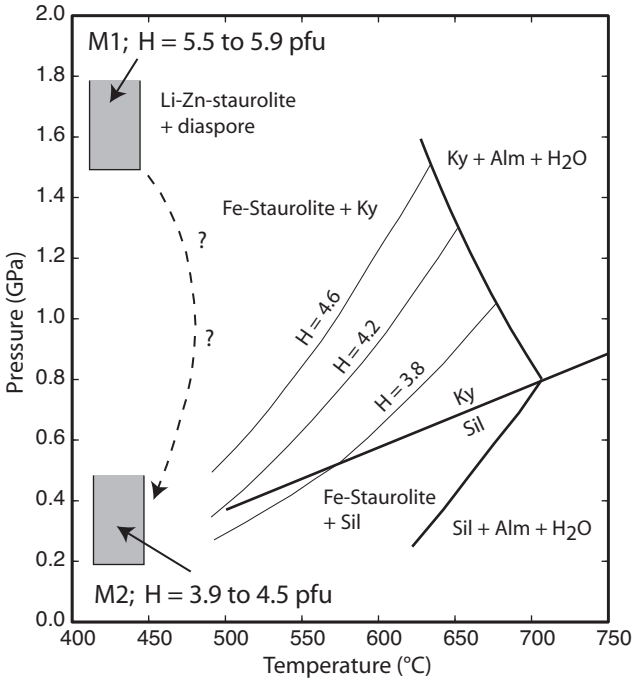

Figure 6. *P-T* plot indicating M1 and M2 stage metamorphic conditions of the Samos rocks, along with H contents (pfu) of core and rim from staurolite Sa9aE. Also given are isopleths of H contents of Fe-staurolite coexisting with kyanite or sillimanite and water (data from Holdaway et al. 1995).

Table headings

Table 1: Preferential sites of cations in the staurolite structure, adapted from Hawthorne et al. (1993c).

Table 2: Representative analyses of staurolite Sa9aE along profiles V-W and S-R. Note:Li and H are measured by SIMS, all other elements by EMP.

Table 1: Preferential sites of cations in the staurolite structure. Adapted from Hawthorne (1993c).

General formula	Cations	Sites
A_4	Fe^{2+}, Mg^{2+}, ❒ (❒ > 2)	M4A, M4B
B_4	Fe^{2+}, Zn^{2+}, Co^{2+}, Mg^{2+}, Li^{+}, Al^{3+}, Mn^{2+}, ❒	T2
C_{16}	Al^{3+}, Fe^{3+}, Cr^{3+}, V^{3+}, Mg^{2+}, Ti^{4+}	M1A, M1B, M2
D_4	Al^{3+}, Mg^{2+}, ❒ (❒ > 2)	M3A, M3B
T_8	Si^{4+}, Al^{3+}	T1
X_8	OH^{-}, F^{-}, O^{2-}	O1A, O1B

Table 2: Representative analyses of staurolite Sa9aE along profiles V-W and S-R. Li and H are measured by SIMS, all other elements by EMP

Profile	Profile V-W											Profile S-R					
Analysis no.	6	12	21	24	26	33	37	43	44	51	58	52	55	66	71	76	84
Distance(µm)	21	39	66	102	114	138	159	183	210	231	252	5	25	115	165	205	250
SiO_2	29,03	28,94	28,94	28,27	28,72	28,54	28,87	28,64	28,79	28,76	29,12	29,66	29,46	29,49	29,21	29,05	29,52
TiO_2	0,11	0,16	0,11	0,16	0,10	0,07	0,06	0,11	0,07	0,21	0,13	0,13	0,09	0,05	0,07	0,15	0,07
Al_2O_3	54,13	53,57	53,78	52,69	52,78	53,47	54,11	53,32	53,43	53,79	54,29	54,85	54,36	54,46	53,98	53,48	55,05
Cr_2O_3	0,09	0,27	0,10	0,09	0,11	0,04	0,01	0,07	0,07	0,23	0,04	0,03	0,06	0,09	0,12	0,01	0,05
FeO	2,20	1,56	1,02	1,07	1,15	0,95	0,92	0,77	0,82	1,18	2,26	2,15	1,90	0,81	0,83	0,85	2,33
MgO	0,19	0,18	0,16	0,25	0,31	0,21	0,14	0,12	0,22	0,16	0,20	0,22	0,16	0,14	0,15	0,31	0,21
MnO	0,18	0,06	0,13	0,14	0,27	0,15	0,11	0,12	0,15	0,14	0,19	0,16	0,11	0,15	0,08	0,16	0,20
ZnO	9,60	11,03	11,85	11,83	11,58	12,41	12,06	12,44	12,44	12,35	9,72	9,54	10,52	12,46	12,54	12,45	9,82
NiO	0,45	0,22	0,26	0,24	0,23	0,28	0,24	0,24	0,25	0,16	0,40	0,30	0,51	0,31	0,29	0,26	0,37
CoO	0,41	0,26	0,05	0,09	0,03	0,04	0,03	0,05	0,03	0,14	0,42	0,39	0,36	0,00	0,08	0,10	0,44
Li_2O	1,08	1,06	1,06	1,03	0,98	1,05	1,10	1,15	1,09	1,07	1,23	0,99	0,99	0,93	0,93	0,89	1,01
H_2O	2,49	2,31	2,74	3,02	3,25	2,76	2,58	2,40	2,56	2,51	2,07	2,52	2,52	2,85	2,83	2,88	2,66
Total	99,96	99,62	100,20	98,88	99,51	99,97	100,23	99,43	99,92	100,70	100,07	100,94	101,04	101,74	101,11	100,59	101,73
Cations on the basis of 48 O, all Fe ferrous																	
Si	7,980	8,022	7,950	7,864	7,910	7,885	7,940	7,973	7,965	7,914	8,032	8,054	8,034	7,984	7,968	7,965	7,971
^{T1}Al	0,020	0,000	0,050	0,136	0,090	0,115	0,060	0,027	0,035	0,086	0,000	0,000	0,000	0,016	0,032	0,035	0,029
$^{T1}Total$	8,000	8,022	8,000	8,000	8,000	8,000	8,000	8,000	8,000	8,000	8,032	8,054	8,034	8,000	8,000	8,000	8,000
Ti	0,024	0,033	0,023	0,034	0,021	0,014	0,012	0,023	0,015	0,043	0,027	0,027	0,018	0,010	0,014	0,032	0,015
$^{T2}Al+^{VI}Al$	17,541	17,502	17,413	17,273	17,135	17,411	17,541	17,491	17,422	17,447	17,645	17,555	17,472	17,380	17,356	17,280	17,520
Cr	0,020	0,060	0,022	0,019	0,023	0,009	0,002	0,015	0,016	0,050	0,010	0,007	0,013	0,019	0,027	0,003	0,011
Fe^{2+}	0,507	0,361	0,234	0,248	0,264	0,220	0,213	0,180	0,190	0,272	0,521	0,487	0,433	0,184	0,190	0,195	0,526
Mg	0,079	0,074	0,065	0,105	0,129	0,085	0,059	0,050	0,090	0,064	0,084	0,089	0,065	0,058	0,062	0,128	0,084
Mn	0,042	0,014	0,031	0,033	0,062	0,035	0,026	0,028	0,035	0,032	0,045	0,037	0,025	0,035	0,019	0,036	0,045
Zn	1,949	2,258	2,405	2,430	2,356	2,532	2,449	2,556	2,541	2,511	1,980	1,912	2,119	2,492	2,526	2,519	1,959
Ni	0,101	0,049	0,058	0,054	0,052	0,063	0,054	0,054	0,056	0,035	0,089	0,065	0,113	0,068	0,063	0,057	0,080
Co	0,090	0,058	0,010	0,020	0,007	0,010	0,006	0,011	0,007	0,031	0,093	0,084	0,079	0,000	0,017	0,022	0,094
Sum R^{2+}	2,767	2,813	2,802	2,890	2,869	2,944	2,806	2,879	2,918	2,944	2,812	2,674	2,834	2,837	2,877	2,958	2,787
Li	1,198	1,186	1,175	1,151	1,088	1,172	1,217	1,285	1,215	1,184	1,361	1,085	1,090	1,011	1,024	0,982	1,095
Sum R^{2+}+ Li	3,964	3,999	3,977	4,042	3,957	4,116	4,023	4,164	4,132	4,128	4,173	3,759	3,924	3,848	3,902	3,939	3,881
H	4,572	4,280	5,027	5,604	5,976	5,087	4,738	4,457	4,716	4,609	3,814	4,556	4,575	5,141	5,145	5,270	4,797
Mole fractions X_i = i / $\sum R^{2+}$+ Li																	
X_{Fe}	0,128	0,090	0,059	0,061	0,067	0,053	0,053	0,043	0,046	0,066	0,125	0,130	0,110	0,048	0,049	0,050	0,135
X_{Mg}	0,020	0,019	0,016	0,026	0,033	0,021	0,015	0,012	0,022	0,015	0,020	0,024	0,017	0,015	0,016	0,032	0,022
X_{Mn}	0,011	0,004	0,008	0,008	0,016	0,008	0,007	0,007	0,008	0,008	0,011	0,010	0,006	0,009	0,005	0,009	0,011
X_{Zn}	0,492	0,565	0,605	0,601	0,595	0,615	0,609	0,614	0,615	0,608	0,474	0,509	0,540	0,648	0,647	0,640	0,505
X_{Ni}	0,025	0,012	0,014	0,013	0,013	0,015	0,013	0,013	0,014	0,008	0,021	0,017	0,029	0,018	0,016	0,015	0,021
X_{Co}	0,023	0,015	0,003	0,005	0,002	0,002	0,002	0,003	0,002	0,007	0,022	0,022	0,020	0,000	0,004	0,006	0,024
X_{Li}	0,302	0,297	0,295	0,285	0,275	0,285	0,303	0,309	0,294	0,287	0,326	0,289	0,278	0,263	0,263	0,249	0,282

Note:Li and H are measured by SIMS, all other elements by EMP.